IOP Publishing Plasma Physics and Controlled Fusion
Plasma Phys. Control. Fusion **63** (2021) 065001 (14pp) https://doi.org/10.1088/1361-6587/abf403

Effects of equilibrium radial electric field on ion temperature gradient instability in the scrape-off layer of a field-reversed configuration

W H Wang[1], J Bao[1], X S Wei[1], Z Lin[1,*], G J Choi[1], S Dettrick[2], A Kuley[3], C Lau[2], P F Liu[1] and T Tajima[1,2]

[1] Department of Physics and Astronomy, University of California, Irvine, CA 92697, United States of America
[2] TAE Technologies, Inc., Foothill Ranch, CA 92610, United States of America
[3] Department of Physics, Indian Institute of Science, Bangalore 560012, India

E-mail: zhihongl@uci.edu

Received 2 November 2020, revised 18 March 2021
Accepted for publication 31 March 2021
Published 20 April 2021

Abstract

Linear and nonlinear effects of the equilibrium radial electric field on the ion temperature gradient (ITG) instability in the scrape-off layer (SOL) of a field-reversed configuration have been studied using gyrokinetic particle simulations for a single toroidal mode. Linear simulations with adiabatic electrons find that the $E \times B$ flow shear reduces the growth rate and causes a radial tilting of the mode structure on the toroidal plane. Nonlinear simulations find that the $E \times B$ flow shear significantly decreases ITG saturation amplitude and ion heat transport in the SOL by reducing both turbulence intensity and eddy size. The turbulence intensity is determined by fluid eddy rotation, which is the dominant saturation mechanism for the SOL ITG instability with a single toroidal mode number. On the other hand, parallel wave-particle decorrelation is the dominant mechanism for the SOL ITG turbulent transport. A random walk model using the guiding center radial excursion as the characteristic length scale and the eddy turnover time as the characteristic time scale fits very well to the scaling of ion heat conductivity with the $E \times B$ flow shear.

Keywords: $E \times B$ shear, ITG mode, turbulence transport, FRC

(Some figures may appear in colour only in the online journal)

1. Introduction

A field-reversed configuration (FRC) is an elongated prolate compact toroid with purely poloidal magnetic field. It consists of two regions with different topologies: an inner core region with closed field lines and an outer scrape-off layer (SOL) with open field lines [1]. The FRC draws research interests because of its engineering advantages as a fusion reactor. Recent progress at the TAE Technologies, Inc. has demonstrated a robust formation and sustainment of the FRC plasmas for tens of milliseconds [2–4]. The confinement of the FRC plasmas is now in a turbulent transport-limited regime thanks to the suppression of major macroscopic instabilities [1, 4]. Therefore, understanding the turbulent transport mechanism in FRC can be important for improving the plasma confinement to fusion-relevant regime.

The macroscopic wobble and rotational instabilities in these FRC experiments are suppressed by a combination of edge biasing, plasma gun, and neutral beam injection (NBI)

* Author to whom any correspondence should be addressed.

[5]. The resulted energetic ion population by NBI helps to stabilize the system because of its large ion finite Larmor radius (FLR) effects [6], a benefit that is usually absent in tokamaks. Meanwhile, microscopic drift-wave turbulence on the scale of thermal ion gyroradius is often suppressed in the FRC core, but ion-to-electron scale drift-wave turbulence in the SOL has been observed from the experiments [7].

Our previous linear local simulations using the gyrokinetic toroidal code (GTC) [8] shows that the suppression of ion-scale drift-waves in the FRC core can be due to large FLR, magnetic well geometry (magnetic pressure gradient and kinetic pressure gradient are in opposite direction), and short electron transit length (short–circuit effect), leaving only electron scale fluctuations in the core [7, 9–11]. The SOL region, on the other hand, does not have those advantages, and thus both electron and ion scale drift-waves can be unstable in the SOL with critical pressure gradient comparable to the experimentally measured threshold [11]. Subsequent nonlinear simulations using the global particle code ANC [12] find that linear drift-wave instabilities first grow in the SOL, then turbulence nonlinearly spreads from SOL to core, resulting in a toroidal wavenumber spectrum consistent with the experimental measurements [13, 14]. The induced transport in the FRC core is also shown to be quite different from tokamaks in these simulations. An upgrade code of GTC developed for global FRC simulations, GTC-X, finds that linear ion temperature gradient modes (ITG) in the SOL are globally connected and axially varying across central FRC region, mirror throat area, and formation exit area [15].

The edge biasing plasma gun and NBI can generate an inward equilibrium radial electric field penetrating through the edge layer and counterbalancing the usual FRC spin-up. Since the ion scale drift-waves only grow in the SOL region, it is natural to use such capabilities as an effective tool for active control and reduction of turbulent transport in the FRC [4, 5, 7]. In fact, the equilibrium $E \times B$ sheared flows in tokamak have been shown to effectively suppress drift-wave turbulence by reducing linear growth rate, nonlinear eddy size, fluctuation intensity, and turbulent transport [16–19]. This motivates our research using gyrokinetic simulations to understand the effects of equilibrium $E \times B$ sheared flow on the turbulent transport in the FRC SOL.

The effects of shear flows have been extensively studied for tokamaks both analytically and numerically. Early paper by Biglari, Diamond and Terry [16] suggests that turbulence can be suppressed when the $E \times B$ shearing rate becomes comparable to the turbulence decorrelation rate. Hahm and Burrell [17] calculates the $E \times B$ shearing rate for fluctuation suppression in the toroidal geometry. Connor *et al* [20] show that the strong sheared rotation cancels effect of toroidal curvature and thus reduces the radial mode width [21]. Waltz *et al* verify in numerical simulations the turbulence quench rule requiring the critical $E \times B$ shearing rate to exceed the maximum of instability growth rates [22]. More recent numerical simulations demonstrate the mode tilting effects associated with sheared flows [23, 24]. Zonal flow is another important contribution to the $E \times B$ sheared flow effects in tokamaks. Lin *et al* show in global gyrokinetic simulation that zonal flow generated by the turbulence substantially reduced the simulated transport [8]. The zonal flow is shown to be generated by the modulational instability [25, 26].

Despite the difference of magnetic field geometry between FRC and tokamaks, we see similar suppression effect of microturbulence by sheared equilibrium flows. We show that for the 2D turbulence with a single toroidal mode, the equilibrium flow shear effectively reduces the linear growth rate of the ITG in the FRC SOL. We also elucidate the mechanism of heat transport through the fluid eddy rotation and kinetic parallel decorrelation. This work provides insights for understanding the effects of biasing electric field in FRC experiments.

In this work, we extend the GTC-X code for simulations with equilibrium radial electric fields for a single toroidal mode. We study linear and nonlinear effects of $E \times B$ sheared flows on the ITG instability in the FRC SOL. Linear simulations with adiabatic electrons find that the $E \times B$ flow shear reduces the growth rate and causes a radial tilting of the mode structure on the toroidal plane. Maximal growth rate with an un-tilted mode structure occurs when the radial shear of the Doppler-shifted local mode frequency is zero. Nonlinear simulations find that the $E \times B$ flow shear significantly decreases ITG saturation amplitude and ion heat transport in the SOL by reducing both turbulence intensity and eddy size. In the absence of self-generated zonal flows, fluid eddy rotation is the dominant saturation mechanism for the SOL ITG instability with a single toroidal mode number, and it determines the nonlinear saturation amplitude. On the other hand, parallel wave-particle decorrelation [27] is the dominant mechanism for the SOL ITG turbulent transport, a physics insight enabling the construction of a random walk model using guiding center radial excursion as the characteristic length scale and eddy turnover time as the characteristic time scale. Finally, our simulation results suggest that maximizing the radial shear of the Doppler-shifted local mode frequency can effectively suppress the ITG instability and associated transport in the FRC SOL.

The rest of the paper is organized as follows. In section 2, we formulate the gyrokinetic simulation model with equilibrium radial electric field and construct an improved gyroaveraging procedure for a single-toroidal-mode simulation in FRC. We verify this simulation model for an equilibrium radial electric field with a rigid rotation in section 3. In section 4, we discuss linear simulation results for the effects of $E \times B$ sheared flows on the single-toroidal-mode ITG instability. We present the nonlinear simulation results for the effects of $E \times B$ sheared flows on the single-toroidal-mode ITG turbulence and ion transport in section 5. Section 6 is a summary of the simulation results and a plan for the future work.

2. Formulation of gyrokinetic simulation model with radial electric field

2.1. Gyrokinetic simulation model

The gyrokinetic formulation holds true when we focus on plasma instabilities with a frequency much smaller than

cyclotron frequency and a gyroradius much smaller than the machine size. Because the gyroradius is relatively large in the FRC core and near the null points of magnetic field in FRC, a fully kinetic approach should be considered for these regions. However, the gyrokinetic assumptions can still be valid in the SOL, since the gyroradius becomes small due to the drastic temperature drop in the edge. Although we may expect a high β (ratio of kinetic pressure to magnetic pressure) value near the FRC core, a typical β in the SOL could be around 0.01 in our simulation. Therefore, when we study the ITG instability in the SOL, the electrostatic gyrokinetic equation can still be used to evolve the ion distribution thanks to its efficiency to capture the low frequency instabilities [28]. By averaging over the fast gyromotion, the long-time-scale ion dynamics can be studied in a reduced five-dimensional phase space $\left(\boldsymbol{R}, v_{\parallel}, \mu\right)$,

$$Lf\left(\boldsymbol{R}, v_{\parallel}, \mu, t\right) = \left(\frac{\partial}{\partial t} + \dot{\boldsymbol{R}} \cdot \nabla + \dot{v}_{\parallel} \frac{\partial}{\partial v_{\parallel}}\right) f\left(\boldsymbol{R}, v_{\parallel}, \mu, t\right) = 0, \tag{1}$$

where $\dot{\boldsymbol{R}} = v_{\parallel}\boldsymbol{b} + \boldsymbol{v}_E + \boldsymbol{v}_d$, $\boldsymbol{v}_E = \frac{c\boldsymbol{b}\times\nabla\delta\phi}{B^*_{\parallel}}$, $\boldsymbol{v}_d = \frac{cm_i v_{\parallel}^2}{Z_i B^*_{\parallel}}\boldsymbol{b} \times (\boldsymbol{b}\cdot\nabla\boldsymbol{b}) + \frac{c\mu}{Z_i B^*_{\parallel}}\boldsymbol{b}\times\nabla B$, $\dot{v}_{\parallel} = -\frac{\boldsymbol{B}^*}{m_i B^*_{\parallel}} \cdot (Z_i\nabla\langle\delta\phi\rangle + \mu\nabla B)$. Here, $\boldsymbol{b} = \frac{\boldsymbol{B}}{B}$ is the unit vector of the equilibrium magnetic field $\boldsymbol{B}$, $\boldsymbol{B}^* = \boldsymbol{B} + \frac{Bv_{\parallel}}{\Omega_i}\nabla\times\boldsymbol{b}$, $B^*_{\parallel} = \boldsymbol{b}\cdot\boldsymbol{B}^*$, and $v_{\parallel}$ is the parallel velocity along magnetic field line. The guiding center position $\boldsymbol{R}$ can be expressed by particle position $\boldsymbol{x}$ and its gyroradius $\boldsymbol{\rho}$, i.e. $\boldsymbol{R} = \boldsymbol{x} - \boldsymbol{\rho} = \boldsymbol{x} - \frac{\boldsymbol{b}\times\boldsymbol{v}_{\perp}}{\Omega_i}$, where $\Omega_{\mathrm{i}} = \frac{Z_i B}{m_i c}$ is ion cyclotron frequency, Z_{i} and m_{i} are the ion charge and mass, respectively. The particle perpendicular velocity is $\boldsymbol{v}_{\perp}$ with a magnitude of $v_{\perp} = \sqrt{\frac{2\mu B}{m_{\mathrm{i}}}}$ with μ being the magnetic moment. The gyrophase α is averaged out when deriving equation (1) [28]. The perturbed electrostatic potential $\delta\phi$ is gyro–averaged through the operator $\langle\delta\phi\rangle = \int\frac{\mathrm{d}\alpha}{2\pi}\int\mathrm{d}\boldsymbol{x}\,(\delta\phi)\,\delta\left(\boldsymbol{x}-\boldsymbol{R}-\boldsymbol{\rho}\right)$.

In order to reduce the particle noise, the perturbative δf method is used [29–32]. The distribution function is divided into an equilibrium part and a time-varying perturbation part, $f = f_0\left(\boldsymbol{R}, v_{\parallel}, \mu\right) + \delta f\left(\boldsymbol{R}, v_{\parallel}, \mu, t\right)$. The equilibrium satisfies the zeroth order equation

$$L_0 f_0 = 0. \tag{2}$$

Here, we also separate the Lagrangian operator into equilibrium and perturbation parts, $L = L_0 + \delta L$, where $L_0 = \frac{\partial}{\partial t} + \left(v_{\parallel}\boldsymbol{b} + \boldsymbol{v}_d\right)\cdot\nabla - \frac{\boldsymbol{B}^*}{m_i B^*_{\parallel}}\cdot\mu\nabla B\frac{\partial}{\partial v_{\parallel}}$ and $\delta L = \boldsymbol{v}_E\cdot\nabla - \frac{\boldsymbol{B}^*}{m_i B^*_{\parallel}}\cdot\left(Z_i\nabla\langle\delta\phi\rangle\right)\frac{\partial}{\partial v_{\parallel}}$. It can be proven that for FRC geometry, $f_0 = n_0\left(\frac{m_{\mathrm{i}}}{2\pi T_0}\right)^{3/2}\exp\left[-\frac{m_i v_{\parallel}^2 + 2\mu B}{2T_0}\right]$ is the exact solution for equation (2), with n_0 and T_0 as a function of magnetic flux ψ. By subtracting equation (2) from equation (1), we can obtain the perturbation equation

$$L\delta f = -\delta L f_0. \tag{3}$$

By defining $w = \frac{\delta f}{f}$, we can then derive the nonlinear weight equation [30]

$$\begin{aligned}\frac{dw}{dt} &= -\frac{1}{f}\delta L f_0 \\ &= (1-w)\left\{-\boldsymbol{v}_E\cdot\left.\frac{\nabla f_0}{f_0}\right|_{v_{\perp}} - \frac{Z_i v_{\parallel}\boldsymbol{b}\cdot\nabla\langle\delta\phi\rangle}{T_0}\right. \\ &\quad \left. - \frac{Z_i}{T_0}\left[\frac{\mu\boldsymbol{b}\times\nabla B_0}{m_i\Omega_i} + \frac{v_{\parallel}^2}{\Omega_i}\boldsymbol{b}\times(\boldsymbol{b}\cdot\nabla\boldsymbol{b})\right]\cdot\nabla\langle\delta\phi\rangle\right\}\end{aligned} \tag{4}$$

where we replace $\nabla f_0|_{\mu}$ by noticing $\nabla f_0|_{v_{\perp}} = \nabla f_0|_{\mu} + \frac{\mu\nabla B}{T_0}f_0$. Using δf solved from equation (4), we can compute the perturbed ion guiding center density

$$\begin{aligned}\langle\delta n\rangle(\boldsymbol{x}, t) = \int\frac{B}{m_i}\mathrm{d}v_{\parallel}\mathrm{d}\mu\int\mathrm{d}\alpha\int\mathrm{d}\boldsymbol{R}\;\delta f\left(\boldsymbol{R}, v_{\parallel}, \mu, t\right) \\ \times\,\delta\left(\boldsymbol{R}+\boldsymbol{\rho}-\boldsymbol{x}\right).\end{aligned} \tag{5}$$

Then, using the gyrokinetic Poisson's equation [33], we can calculate the perturbed electrostatic potential

$$\frac{Z_i^2 n_0}{T_0}\left(\delta\phi - \widetilde{\delta\phi}\right) = Z_i\langle\delta n\rangle - e\delta n_e. \tag{6}$$

The left hand side of equation (6) is ion polarization density with the double gyro-phase-averaged term defined as

$$\begin{aligned}\widetilde{\delta\phi}(\boldsymbol{x}, t) = \frac{1}{n_0}\int\frac{B}{m_i}\mathrm{d}v_{\parallel}\mathrm{d}\mu\int\mathrm{d}\alpha\int\mathrm{d}\boldsymbol{R}\,f_0\left(\boldsymbol{R}, v_{\parallel}, \mu, t\right) \\ \times\,\langle\delta\phi\rangle\delta\left(\boldsymbol{R}+\boldsymbol{\rho}-\boldsymbol{x}\right).\end{aligned} \tag{7}$$

In this work, we assume a simple adiabatic response for electrons, i.e. $\delta n_{\mathrm{e}} = n_{\mathrm{e}0}\frac{e\delta\phi}{T_{\mathrm{e}0}}$, and Padé approximation is used to compute $\widetilde{\delta\phi}$ [15, 34].

2.2. Equilibrium radial electric field

In this section, we provide a simple formulation for incorporating equilibrium radial electric field E_r, where r represents minor radius in the FRC geometry. To add the equilibrium radial electric field into our formulation, the electric field should be generalized to include an equilibrium part, i.e. $\phi = \delta\phi + \phi_{\mathrm{eq}}$, where the equilibrium electrostatic potential ϕ_{eq} is a function of poloidal flux ψ only. The gyrokinetic equation becomes,

$$\begin{aligned}Lf = \frac{\partial f}{\partial t} + \left(v_{\parallel}\boldsymbol{b} + \boldsymbol{v}_E + \boldsymbol{v}_{\mathrm{eq}} + \boldsymbol{v}_{\mathrm{d}}\right)\cdot\nabla f \\ - \left[\frac{\boldsymbol{B}^*}{m_i B^*_{\parallel}}\cdot\left(Z_i\nabla\langle\delta\phi\rangle + Z_i\nabla\phi_{\mathrm{eq}} + \mu\nabla B\right)\right]\frac{\partial f}{\partial v_{\parallel}} = 0.\end{aligned} \tag{8}$$

Here, the equilibrium quantities like ϕ_{eq} are not gyro-averaged, because we assume that the length scale of such equilibrium changes is much larger than the gyroradius, i.e.

$\rho/R_0 \approx 0.035$, where R_0 is the major radius of the magnetic axis. Notice that in the ideal FRC, we have the relations,

$$B_R = -\frac{1}{R}\frac{\partial \psi}{\partial Z},\ B_Z = \frac{1}{R}\frac{\partial \psi}{\partial R},\ B_\zeta = 0 \tag{9}$$

where (R,ζ,Z) is the cylindrical coordinates of the guiding center with Z pointing in axial direction. The two equilibrium terms related to $\phi_{\rm eq}$ in equation (8) are $\boldsymbol{v}_{\rm eq} = \frac{c\boldsymbol{b}\times\nabla\phi_{\rm eq}}{B} = R\frac{{\rm d}\phi_{\rm eq}}{{\rm d}\psi}\hat{\boldsymbol{\zeta}}$ and $\frac{\boldsymbol{B}^*}{m_i B_\parallel^*}\cdot(\,Z_i\nabla\phi_{\rm eq}) = 0$, since $\nabla\times\boldsymbol{b}$ is in the ζ-direction. Eventually, the only modification is to add an extra term in equilibrium L_0, i.e.,

$$L_0 = \frac{\partial}{\partial t} + \left(v_\parallel \boldsymbol{b} + \boldsymbol{v}_{\rm eq} + \boldsymbol{v}_{\rm d}\right)\cdot\nabla - \frac{\boldsymbol{B}^*}{m_i B_\parallel^*}\cdot\mu\nabla B\frac{\partial}{\partial v_\parallel}. \tag{10}$$

Notice that even after including E_r term, the local Maxwellian f_0 we obtained for equation (2) is still an exact solution for this new formulation since $\phi_{\rm eq}$ is a function of ψ only.

The above derivation is only valid for a weak E_r field, i.e. when $v_{\rm eq}$ is much smaller than the ion thermal speed. A more rigorous derivation with strong $E\times B$ drift up to thermal velocity has been discussed for the tokamak geometry [35–37]. Comparing to the general formulation discussed in the tokamak case, we can see the $\nabla\times\boldsymbol{v}_{\rm eq}$ and $\nabla\left(v_{\rm eq}^2\right)$ terms are dropped out in our formulation for a weak $E\times B$ drift. In the future work, the more rigorous formulation for E_r effects should be taken into account for stronger $E\times B$ drift.

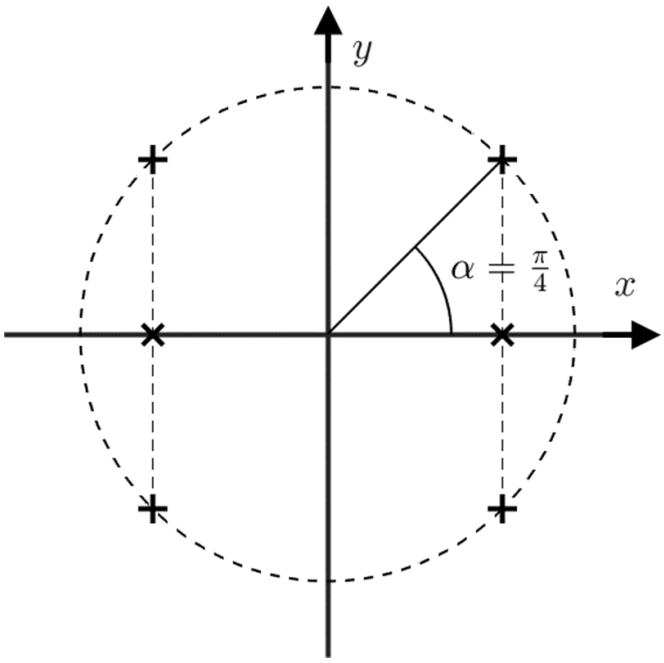

Figure 1. A sketch for cyclotron orbit (dashed circle) in a local Cartesian coordinates (x,y) for the new gyro-averaging procedure. The gyro-averaged value $\langle\phi\rangle$ at the guiding center position $(0,0)$ is the average of $\phi_n(x)J_0(k_y\rho)$ at the two points marked with 'x', each of which is equivalent to the average of ϕ at the two points connected by the vertical dashed lined and marked with '+'.

2.3. Gyro-averaging procedure for a single toroidal mode

To accurately include the FLR effects, a numerical method of gyro-averaging is developed for a single toroidal mode with a perpendicular wavelength on the order of gyroradius. The standard method of the four-point averaging [33] is not efficient for the FRC geometry due to the toroidal domain-decomposition in the GTC-X parallelization. In the previous GTC-X simulations, the gyro-averaging is implemented by multiplying perturbed quantities with a Bessel function assuming that the perpendicular wavevector is dominated by the toroidal component. To include radial component of the wavevector, the gyro-averaging procedure is upgraded in this section by combining the Bessel function for the toroidal wavevector and a radial gyro-averaging, which only involves perturbed quantities on a single toroidal plane. By doing so, we can avoid the data transfer between different toroidal domains during parallel computation. In the future, we will extend this method into multiple-toroidal-mode simulation. A straightforward way is to apply such single-mode procedure for each toroidal mode.

GTC-X uses the cylindrical coordinates $(R,\,\zeta,\,Z)$ to describe the particle dynamics and the field quantities in the global FRC geometry. For the gyro-averaging procedure, we define a local Cartesian coordinate system $(x,\,y,\,z)$ with the origin at the guiding center position. We can choose the z-direction parallel to the magnetic field direction, the y-direction in the toroidal ζ-direction, and the x-direction in the direction perpendicular to the flux surface (i.e. in the radial R-direction if the guiding center position is at $Z=0$). A charged particle with a gyroradius $\rho = v_\perp/\Omega_{\rm i}$ has a cyclotron orbit close to a circle of $(x,\,y) = (\rho\cos\alpha, \rho\sin\alpha)$ with a gyrophase α. A sketch of the gyromotion on the $(x,\,y)$ plane at $z=0$ is given in figure 1.

For a single toroidal mode number $n = Rk_\zeta$, the perturbed electrostatic potential on the gyromotion plane of $z=0$ can be expressed as $\phi(x,y) = \phi_n(x)\,{\rm e}^{ik_y y}$, where $k_y = k_\zeta$ in the local Cartesian coordinates. The gyro-averaged potential at the guiding center position is $\langle\phi\rangle = \langle\phi(x=\rho\cos\alpha, y=\rho\sin\alpha)\rangle = \frac{1}{2\pi}\int_0^{2\pi}{\rm d}\alpha\ \phi_n(\rho\cos\alpha)\,{\rm e}^{ik_y\rho\sin\alpha}$. In previous simulations [15], radial variations of the potential are neglected in the gyro-averaging so $\langle\phi\rangle = J_0(k_y\rho)\,\phi_n(x=0)$. Since the radial direction is not a symmetric direction, GTC-X does not use the spectral representation in the radial direction. So, the gyro-averaging cannot use the Bessel function with a radial wavevector.

To take into account the radial variations over the scale length on the order of the gyroradius, we can construct a new gyro-averaging procedure combining the toroidal averaging with $J_0(k_y\rho)$ and a two-point radial averaging with a distance Δx on both sides of the guiding center position:

$$\langle\phi\rangle = \frac{1}{2}J_0(k_y\rho)\left[\phi_n(\Delta x) + \phi_n(-\Delta x)\right]. \tag{11}$$

The distance Δx is determined by making equation (11) as close as possible to the true gyro-averaged value. For the pur-

pose of finding the optimal value of Δx, we assume the radial variations as $\phi_n(x) = \Phi_n e^{ik_x x}$. Then

$$\begin{aligned}\langle\phi\rangle &= \frac{1}{2}J_0(k_y\rho)\,\Phi_n\left[e^{ik_x\Delta x} + e^{-ik_x\Delta x}\right] \\ &= \Phi_n J_0(k_y\rho)\left[J_0\left(\sqrt{2}k_x\Delta x\right) + O(J_4)\right] \end{aligned} \quad (12)$$

where $O(J_4)$ represents terms on the order of J_4. If we choose $\Delta x = \rho/\sqrt{2}$, the gyro-averaged potential becomes:

$$\langle\phi\rangle = \Phi_n J_0(k_y\rho)\left[J_0(k_x\rho) + O(J_4)\right] = \Phi_n J_0(k_\perp\rho)\left[1 + O(J_4)\right] \quad (13)$$

where $k_\perp^2 = k_x^2 + k_y^2$. Therefore, the deviation from the true gyro-averaged value $\langle\phi\rangle = \phi_n J_0(k_\perp\rho)$ is on the order of J_4, which is small for $k_\perp\rho \leqslant 2$ [33]. This procedure of radial gyro-averaging can be applicable for simulations with multiple toroidal mode numbers in the future.

We now show that this new gyro-averaging procedure is equivalent to the standard four-point gyro-averaging. Similar to the radial averaging, a two-point toroidal averaging with $\Delta y = \rho/\sqrt{2}$ gives:

$$\begin{aligned}&\frac{1}{2}\left[\phi(\pm\Delta x, \Delta y) + \phi(\pm\Delta x, -\Delta y)\right] \\ &\quad = \phi_n(\pm\Delta x)\left[J_0(k_y\rho) + O(J_4)\right]. \end{aligned} \quad (14)$$

So each of the potentials $J_0(k_y\rho)\,\phi_n(\pm\Delta x)$ in equation (11), marked with 'x' in figure 1, is simply the two-point toroidal average of the $\phi(\pm\Delta x, \pm\Delta y)$ at the points marked with '+', which are separated from the 'x' points by a distance of $\Delta y = \rho/\sqrt{2}$. Therefore, the gyro-averaged value $\langle\phi\rangle$ of equation (11) is equivalent to the average of the potentials ϕ on the four points with the gyrophase of $\alpha = \pm\pi/4, \pm 3\pi/4$, which are marked with '+' in figure 1.

When implementing this gyro-averaging procedure in the GTC-X, it is straightforward to find the particle position $(\pm\Delta x)$ in a field-aligned mesh in a poloidal plane (ψ, S), where ψ is the poloidal flux and S represents the distance along the magnetic field line at a given ψ. However, such calculations for all particles at every time step are computationally expensive. To reduce the computational cost, we can find the particle position $(\pm\Delta x)$ using a linear interpolation by assuming that the gyroradius is much shorter than the scale length of the equilibrium magnetic field. We first calculate the change in the poloidal flux $\Delta\psi_i$ that corresponds to Δx for a thermal particle with a magnetic moment μ_0 at each grid point i at the beginning of the simulation. For a guiding center with a magnetic moment μ and close to the grid point i, the position of the particle can be calculated by $\Delta\psi = \Delta\psi_i\sqrt{\mu/\mu_0}$ for subsequent time steps.

The gyro-averaging of equation (11) can be extended to a shorter wavelength regime ($k_\perp\rho \geqslant 2$) by adding more points to the radial averaging. However, this technique is invalid near magnetic null or magnetic separatrix of the FRC where the gyroradius can be comparable to the scale length of the magnetic field and thus fully kinetic approach using 6D Vlasov equation is more appropriate.

3. Verification of gyrokinetic simulation model with radial electric field

3.1. Linear simulation of SOL ITG without radial electric field

To demonstrate the effects of the extended gyro-averaging method in the previous section, we first carried out linear simulations of the ITG in the SOL using the same magnetic geometry and plasma profiles as in Bao *et al* [15], which is calculated by a 2D axisymmetric LR_eqMI equilibrium code [38]. Such linear GTC–X simulation has been benchmarked with ANC code [12–15] and GKD1D code [39] showing good agreements. The main structure of GTC-X is developed based on GTC, which is used in early studies for local flux surface simulation that was validated by measurements of the C-2 device at TAE [7]. The deuterium ion gyrokinetic equation is solved using equations (1)–(4) and the electron response is assumed to be adiabatic. The nonlinear perpendicular drift and parallel acceleration due to the perturbed electric fields in equations (1)–(4), and the nonlinear factor $(1-w)$ in the weight equation, i.e. equation (4), are all neglected in the linear simulations.

GTC-X simulation using the new gyro-averaging method for the ITG with a single toroidal mode number $n = 20$, which corresponds to $k_\zeta\rho_i = 0.364$, gives a linear frequency $\omega = -0.251\frac{C_s}{R_0}$ and a growth rate $\gamma = 0.0494\frac{C_s}{R_0}$, where R_0 is the radial position of the magnetic axis in the cylindrical coordinates and C_s is the sound speed defined as $C_s = \sqrt{T_{e0}/m_i}$ with T_{e0} the electron temperature and m_i the ion mass. This result is consistent with the previous simulation without radial gyro-averaging, which gives the results of $\omega = -0.245\frac{C_s}{R_0}$ and $\gamma = 0.0549\frac{C_s}{R_0}$. The 10% decrease in growth rate can be expected due to the radial gyro-averaging effects. The ITG propagates in the ion diamagnetic direction (i.e. negative frequency) and the mode structure of the electrostatic potential is radially tilted (see figure 7(a)) in the equatorial plane ($Z = 0$) due to the radial variations of the ion diamagnetic flows. In the following discussion, the coordinates (R, Z) are always normalized by R_0.

The simulation domain is the same as in Bao *et al* [15]. The total domain length is $Z \in [-9.37, 9.37]$ for simulation of the confinement vessel with a periodic boundary in the axial direction, and ψ ranges from $\psi(R = 1.70, Z = 0)$ to $\psi(R = 2.40, Z = 0)$ which is restricted solely in the SOL region where the ITG mode peaks in previous study. The simulation uses a mesh grid with 80 radial grid number, 32 toroidal grids, 64 parallel grids, and 800 marker particles based on the studies of numerical convergence.

To study the E_r effects, we continue to use the same magnetic geometry, but construct new temperature and density profiles with minimal radial variations of the ion diamagnetic flows to obtain an ITG mode structure with minimal radial tilting, which is usually the most unstable mode given an averaged pressure gradient. As shown in figure 2, the constructed density profile is $n(\psi) = n_0\left[1 + C_{n1}\left(\tanh\frac{\psi_0-\psi}{\Delta\psi} - 1\right)\right]$ and the ion temperature profile is $T(\psi) = T_0\left[1 + C_{T1}\left(\tanh\frac{\psi_0-\psi}{\Delta\psi} - 1\right)\right]$. The corresponding

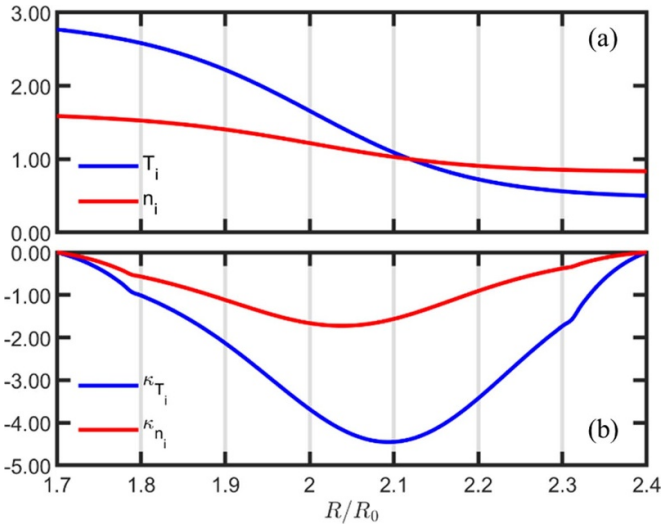

Figure 2. Constructed SOL radial profiles of equilibrium ion density $n_{\rm i}$ and temperature $T_{\rm i}$ (panel (a)) and their radial gradients (panel (b)). All quantities are normalized by their values at the surface with $R = 2.12$ and $Z = 0$.

coefficients are chosen as $n_0 = 15.0$, $C_{n1} = 0.25$, $T_0 = 1.0$, $C_{T1} = 0.42$, $\psi_0 = 1.5$, and $\Delta\psi = 0.75$. These are all dimensionless values with the normalization: reference density by $n_{\rm e0} = 1.22 \times 10^{12}{\rm cm}^{-3}$, reference temperature by $T_{\rm e0} = 80\,{\rm eV}$, and ψ by $\psi_{\rm unit} = B_0 R_0^2$, where $B_0 = 531{\rm G}$ and $R_0 = 26.8$ cm. The electrostatic potential is renormalized as $\frac{e\delta\phi}{T_{\rm e0}}$.

Compared to the original profiles [15], we can see from figure 2 that there is a peak gradient in the central simulation domain around $R = 2.1$ with a relatively flat top. The gradient at the boundary is artificially suppressed to reduce the influence of non-physical boundary effects. GTC-X simulation using the new constructed profiles for the ITG with $n = 20$ gives a linear mode structure with a minimal radial tilting as shown in figure 4(a). The ITG linear frequency is $\omega = -0.251\frac{C_{\rm s}}{R_0}$ and the growth rate is $\gamma = 0.0716\frac{C_{\rm s}}{R_0}$.

The parallel mode spectrum is also computed at each flux surface and shown in panel (a) in figure 5 (discussed in section 4). The maximal ITG mode amplitude occurs at a radial location of $R = 2.12$, which is close to the peak pressure gradient location. Apparently, the dominant parallel mode number is $m = 1$ throughout the radial simulation domain. Taking $m = 1$ as the parallel wavevector $k_\parallel$ and using temperature and density gradients at the mode location, we can derive a slab ITG model [15] with a theoretical dispersion relation of $\omega_{\rm slab} = -0.227\frac{C_{\rm s}}{R_0}$ and $\gamma_{\rm slab} = 0.0544\frac{C_{\rm s}}{R_0}$, which are close to that obtained in the simulation. That is, the long wavelength ITG instability in the SOL observed in the GTC-X simulation is a slab-like mode driven by the parallel resonance with the ions since $|\omega| \sim k_\parallel v_{\rm th} = 0.275$.

3.2. Simulation of SOL ITG with rigid rotation due to radial electric field

We now add an equilibrium radial electric field $\phi_{\rm eq}$ to the ITG simulations discussed in section 2.2 and verify that a rigid rotation due to the $E \times B$ flow only causes a Doppler shift in the ITG frequency with little changes in the growth rate.

The equilibrium radial electric field $E_r = -\nabla\phi_{\rm eq}(\psi)$ in the SOL induces an $E \times B$ flow with a toroidal angular frequency $\Omega_{\rm eq}(\psi)$,

$$\Omega_{\rm eq}(\psi) = \frac{{\rm d}\phi_{\rm eq}}{{\rm d}\psi}. \tag{15}$$

The effects of this sheared $E \times B$ rotation on the microturbulence can be captured by the shearing rate $\omega_{\rm s}(\psi)$ calculated from a two-point nonlinear analysis [17],

$$\omega_{\rm s} = \frac{\Delta\psi}{\Delta\zeta}\frac{\partial\Omega_{\rm eq}}{\partial\psi} = \frac{\Delta\psi}{\Delta\zeta}\frac{{\rm d}^2\phi_{\rm eq}}{{\rm d}\psi^2} \tag{16}$$

where $\Delta\psi$ and $\Delta\zeta$ are the turbulence correlation lengths in radial and toroidal direction, respectively. For an isotropic turbulence eddy ($\Delta R \sim R\Delta\zeta$) near equatorial plane ($Z = 0$), the shearing rate can be simplified to the radial variation of the toroidal rotation frequency,

$$\omega_{\rm s} \approx R^2 B_Z \frac{{\rm d}^2\phi_{\rm eq}}{{\rm d}\psi^2} = \left.\frac{\partial\Omega_{\rm eq}}{\partial\ln R}\right|_{Z=0}. \tag{17}$$

The equilibrium radial electric fields $\boldsymbol{E}_{\rm r}$ are expected to induce a Doppler frequency shift due to the toroidal rotation $\Omega_{\rm eq}$ and a suppression of the drift-wave instabilities due to the rotation shear $\omega_{\rm s}$. To verify our simulation model with the equilibrium electric fields, we first simulate the ITG in the SOL with a rigid rotation by imposing an external electric fields such that $\Omega_{\rm eq} = \frac{{\rm d}\phi_{\rm eq}}{{\rm d}\psi} = $ constant, which will induce a frequency shift of the ITG mode, $\omega \to \omega + n\Omega_{\rm eq}$. The effects of the rigid rotation on the growth rate and mode structure are expected to be small if the $E \times B$ flow speed is much smaller than the ion thermal speed so that the centrifugal force and Coriolis force can be neglected.

We have verified this Doppler frequency shift in our simulations for the rigid rotation frequencies up to the ITG frequency in the absence of the radial electric field, i.e. $\Omega_{\rm eq} = |\omega| = 0.251\frac{C_{\rm s}}{R_0}$, which induce the ITG frequency shifts up to $n\Omega_{\rm eq}$ but less than 5% changes of the growth rates.

4. Effects of $E \times B$ shear on linear single-toroidal-mode ITG instability in SOL

Building on the verification of the simulation with a rigid rotation, we now study effects of the sheared rotation on the single-n-mode linear ITG instability in the SOL by imposing an equilibrium electrostatic potential with a constant shearing rate $\omega_{\rm s}$,

$$\phi_{\rm eq} = \frac{\omega_{\rm s}}{2B_0R_0^2}(\psi - \psi_0)^2 \tag{18}$$

where ψ_0, B_0, R_0 represent values at the radial location with the largest ITG amplitude ($\psi_0 = 2.00$, $B_0 = 1.87$ and $R_0 = 2.12$ is measured at $Z = 0$). The rotation frequency $\Omega_{\rm eq}(\psi_0) = 0$ at the maximal mode amplitude to minimize the Doppler frequency

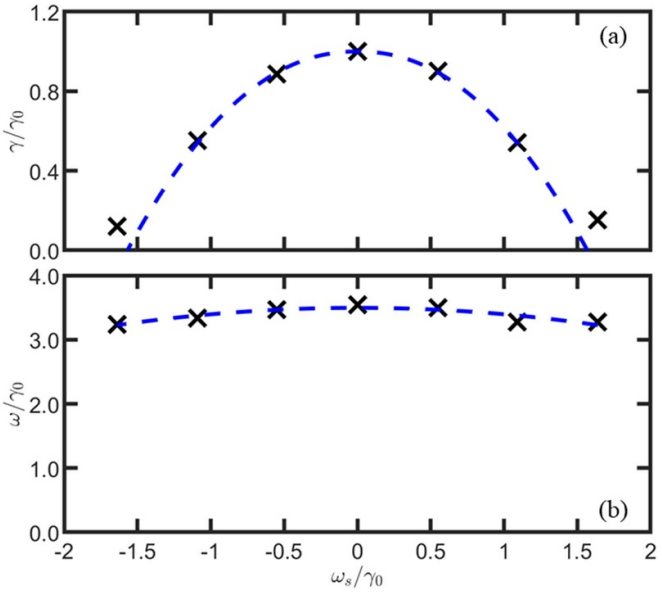

Figure 3. Dependence of SOL ITG growth rate γ (panel (a)) and real frequency ω (panel (b)) on shearing rate ω_s from GTC-X simulations using constructed equilibrium profiles with small radial variations of pressure gradients as shown in figure 2. Dashed lines are fitting curves based on simulation data points ('x').

shift. The maximal $E \times B$ flow speed occurs at the boundaries of the simulation domain and is less than 5% of the ion thermal speed.

We first perform a series of linear simulations of the $n = 20$ ITG in the SOL using the constructed plasma profiles shown in figure 2 with various shearing rates $\omega_s/\gamma_0 = [-1.64,\ 1.64]$. In the following sections, the shearing rate is always normalized to the initial growth rate γ_0 at $\omega_s = 0$ if not specified. Figure 3(b) shows that real frequency changes little because the $E \times B$ rotation frequency is zero at the maximal mode amplitude location. On the other hand, the growth rate decreases significantly with increasing shearing rate and exhibits a symmetry with respect to the sign of the shearing rate ω_s, as shown in figure 3(a). For example, the growth rate decreases to $\gamma/\gamma_0 \sim 0.55$ when $|\omega_s|/\gamma_0 = 1.1$, and to $\gamma/\gamma_0 \sim 0.18$ when $|\omega_s|/\gamma_0 = 1.6$. The dependence of the growth rate on the shearing rate can be fitted by a simple power law $\gamma/\gamma_0 = 1 - C(\ |\omega_s|/\gamma_0)^{\alpha}$, with fitting constants $C = 0.382$ and $\alpha = 2.139$. The suppression of the ITG instability by the $E \times B$ shear in the SOL is slightly weaker than that in the tokamak [40], which might be due to the absence of the toroidal coupling in the FRC with no magnetic shear.

The reduction of the ITG growth rate by the equilibrium $E \times B$ shear is correlated with the radial tilting of the ITG mode structure in the SOL. In figures 4(a)–(c), we plot the electrostatic potentials $\delta\phi$ on the $(R,\ \zeta)$ plane at $Z = 0$ for the entire simulation domain of $R = [1.70,\ 2.40]$ and $\zeta = [0,\ \pi/10]$. Without $E \times B$ flow ($\omega_s = 0$), the mode mostly lines up in the radial direction with little radial tilting (i.e. ground radial eigenstate) since there is little radial shear of the ion diamagnetic flows. The ITG mode propagates in the ion diamagnetic direction (defined as the negative ζ-direction). With a modest shearing rate $\omega_s = 0.55$, the mode structure is tilted in the radial direction. This is induced by the equilibrium $E \times B$ sheared flows negative in the ζ-direction near the inner boundary and positive near the outer boundary, which causes a radial variation of the local wave phase velocity resulting in a mode structure tilting toward positive ζ-direction at the large radial R location. Similarly, a negative shearing rate $\omega_s = -0.55$ results in a mode structure with a negative radial tilting. The ITG growth rate is independent of the tilting direction because of the toroidal symmetry. The radial tilting of the mode structure is even more pronounced for a larger shearing rate of $\omega_s = 1.64$. The large tilting strongly stretches the mode so that the toroidal mode width is larger than the toroidal wavelength, resulting in an oscillation of the potential in the radial direction (i.e. excited radial eigenstate).

The appearance of a large k_r due to the radial tilting by a large shearing rate ω_s can also be seen in the $\delta\phi$ contour plot in the $R - Z$ poloidal plane, as shown in lower panels of figures 4(d)–(f) for the cases of $\omega_s = 0.0,\ 0.55,\ 1.64$. The excited radial eigenstate with a large k_r can be seen clearly for the cases of $\omega_s = 1.64$ in figure 4(f). The radial tilting also induces a radial variation of the parallel wavevector (i.e. poloidal m-spectrum), which may affect wave-particle resonance. In figure 5, the poloidal spectrum is calculated based on the mode structure shown in figures 4(d)–(f). As the shearing rate increases, the radial width of each poloidal harmonic is clearly reduced due to the radial tilting, which leads to a larger k_r. For the cases of $\omega_s = 0.0,\ 0.55$, the radial eigenstate is a ground state, i.e. none of the poloidal harmonics have a null point (except at radial boundaries). For the largest shearing rate $\omega_s = 1.64$, all poloidal harmonics exhibit radial oscillations, i.e. an excited radial eigenstate. Finally, the amplitude ratio of the high-m ($m > 1$) harmonics to the dominant $m = 1$ harmonic increases with the shearing rate, i.e. the $E \times B$ shear enhances the high $k_{\|}$ components of the ITG mode, which could increase the Landau damping and thus reduce the growth rate.

The finding that the radial tilting of the mode structure reduces the ITG growth rate has been further confirmed in GTC-X simulations in the SOL using the same equilibrium radial electric fields of equation (18), but using the original temperature and density profiles in Bao *et al* [15] with a large radial shear of the ion diamagnetic flows. Figure 6(a) shows that the maximal growth rate $\gamma = 0.0629$ occurs at an $E \times B$ shearing rate of $\omega_s = -0.69$, instead of the case of $\omega_s = 0$. The growth rate does not exhibit a symmetry with respect to the sign of the shearing rate ω_s. Figure 6(b) shows that real frequency changes more significantly than that in figure 3(b) since the $E \times B$ rotation frequency in this case is not zero at the radial location of maximal mode amplitude. Because the $E \times B$ rotation frequency at the radial location of maximal mode amplitude depends on the sign of the shearing rate and ψ_0 in equation (18), the frequency does not exhibit a symmetry with respect to the sign of the shearing rate.

In the absence of equilibrium radial electric fields $\omega_s = 0$, the mode structure is strongly tilted in the radial direction for the electrostatic potentials $\delta\phi$ on the $(R,\ \zeta)$ plane at $Z = 0$ as shown in figure 7(a), which is induced by the large radial shear of the ion diamagnetic flows. On the other hand, for the case

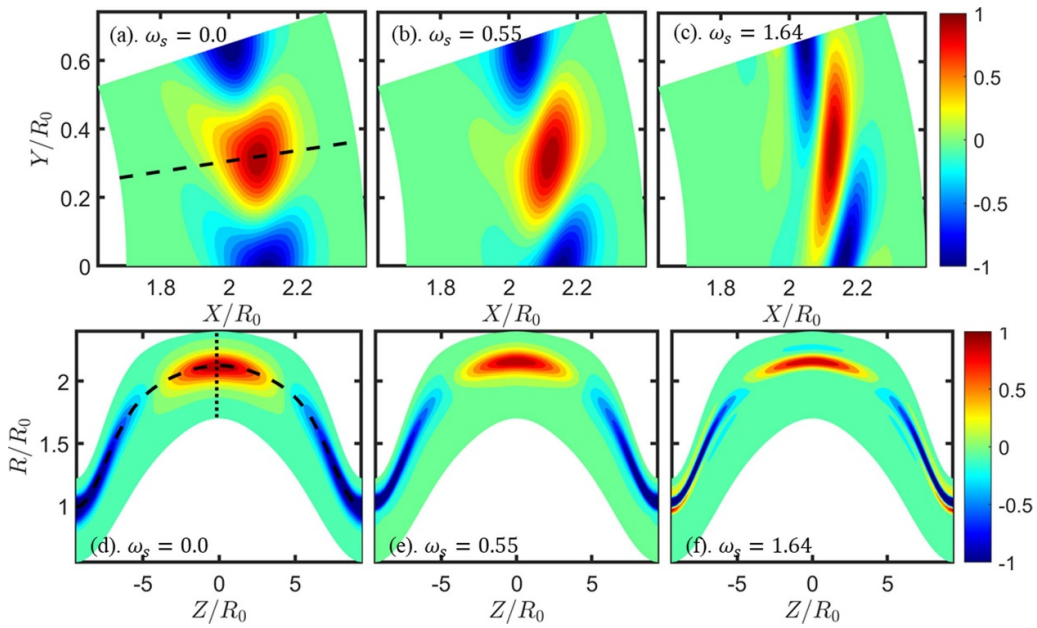

Figure 4. Upper panels (a)–(c) are contour plots of electrostatic potential $\delta\phi$ at the $Z = 0$ toroidal plane from GTC-X simulations in the SOL using constructed equilibrium profiles as shown in figure 2. Equilibrium radial electric fields are imposed with different $E \times B$ shearing rate: (a). $\omega_s = 0.00$, (b). $\omega_s = 0.55$, and (c). $\omega_s = 1.64$. In the figure, $X = R\cos\zeta$ and $Y = R\sin\zeta$. Lower panels (d)–(f) are corresponding eigenmode structure on the poloidal plane. In panel (a), the dashed line is a cut for the poloidal planes appearing in panels (d)–(f). The dashed line in the panel (d) represents the flux surface of the maximal mode amplitude and the vertical dotted line gives the toroidal planes plotted in the upper panels (a)–(c) and the reference line for all 1d radial profiles. All potentials $\delta\phi$ are normalized by their maximal values $\delta\phi_{\max}$.

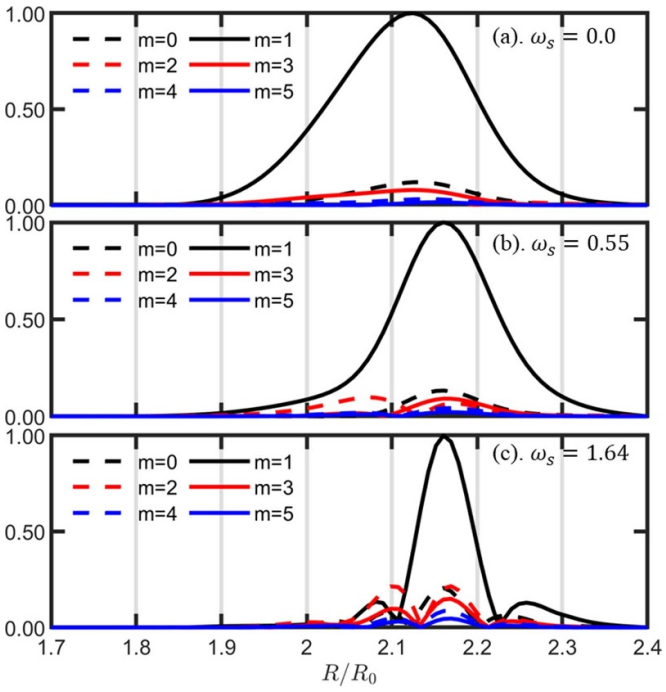

Figure 5. Radial profiles for poloidal harmonics of perturbed potential $\delta\phi$ for simulations using shearing rates corresponding to that in figures 4(d)–(f).

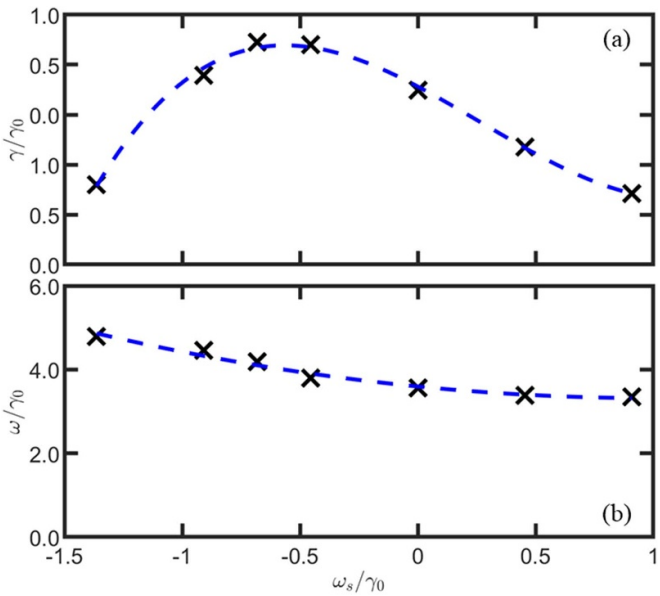

Figure 6. Dependence of ITG growth rate γ (panel (a)) and real frequency ω (panel (b)) on shearing rate ω_s from GTC-X simulations in the SOL using equilibrium profiles with large radial shear of ion diamagnetic flows in Bao *et al* [15]. Dashed lines are fitting curves based on the simulation data points ('x'). All quantities are normalized by $\gamma_0 = 0.0716\frac{C_s}{R_0}$.

of maximal growth rate with $\omega_s = -0.69$, the mode structure mostly lines up in the radial direction with little radial tilting as shown in figure 7(b). These lead us to think that the effects of the radial shear of the $E \times B$ flows compensate the shear of the ion diamagnetic flows. When this happens, one might expect that the radial shear of the sum of the ion diamagnetic

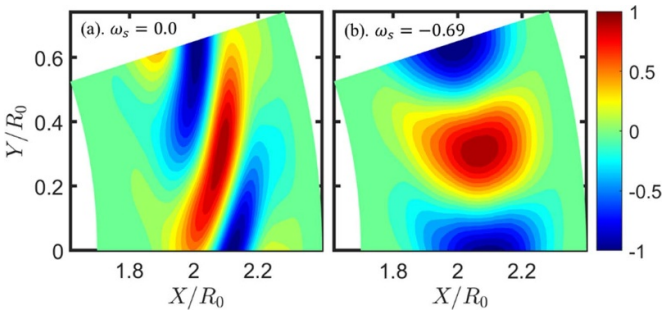

Figure 7. Contour plots of electrostatic potential $\delta\phi$ at the $Z = 0$ toroidal plane from GTC-X simulations in the SOL using the original equilibrium profiles in Bao *et al* [15]. Equilibrium radial electric fields are imposed with different $E \times B$ shearing rate: (a). $\omega_s = 0.0$, (b). $\omega_s = -0.69$. In the figure, $X = R\cos\zeta$ and $Y = R\sin\zeta$.

flows and the $E \times B$ flows is zero. However, the radial shear of the ion diamagnetic flows is much larger than the added $E \times B$ flow shear of $\omega_s = -0.69$ in the simulation. We find that the more relevant quantity is the radial shear of the local mode frequency, which is much smaller than and mostly induced by the diamagnetic flow shear in the absence of the equilibrium radial electric field. Using the simple slab model in section 3.1, we find that $\frac{d\omega_{slab}}{dlnR} = 16.4\gamma_0 \sim n\omega_s$ at $R = 2.1$ for the original profiles. Therefore, the maximal growth rate occurs when the radial shear of the Doppler shifted local mode frequency is zero, i.e. $\frac{d}{dlnR}(\omega_{slab} + n\Omega_{eq}) \sim 0$. For the other case with constructed profiles (figure 2) with minimal radial shear of diamagnetic flows, the radial shear of the local mode frequency is very small in the absence of the equilibrium radial electric field. These results are very similar to that in tokamaks. Abdoul *et al* [24] showing a similar requirement for zero gradient of local mode frequency for the maximal growth rate. The interplay between the diamagnetic flow shear and $E \times B$ flow shear is also discussed by Hill *et al* [23]. Interestingly, in a DIII-D tokamak research [41], the shear in the poloidal group velocity of the turbulent eddy flow near the plasma edge has also been found to be important in the *L–H* confinement transition.

5. Effects of $E \times B$ shear on single-toroidal-mode ITG turbulence and transport in SOL

Building on the GTC-X linear simulations of the ITG instability with $n = 20$, we now carry out nonlinear simulations to study the effects of equilibrium $E \times B$ sheared flows on the single-mode ITG turbulence and transport in the SOL. The ion guiding center equations of motion include the nonlinear perpendicular drift and parallel acceleration due to the perturbed electric fields in equation (1), and the nonlinear factor $(1 - w)$ in the weight equation, equation (4). The simulation domain is the same as used in linear simulation with a single toroidal mode number, $n = 20$.

In the nonlinear simulations, the ion temperature profiles could be relaxed due to heat transport (i.e. temperature gradient becomes smaller in the turbulence region), which could cause the turbulence intensity and heat conductivity to gradually decrease after the nonlinear saturation. To prevent the profile relaxation, an artificial heat bath previously implemented in the GTC [42] has been implemented in the GTC-X. Another nonlinear effect that can cause a gradual decrease of the transport is the formation of small-scale coherent structures in the phase space due to the nonlinear wave-particle trapping, which could easily be destroyed by Coulomb collisions. We have implemented a pitch-angle collision operator [43] in the GTC-X to extend the period of the steady state turbulence after the nonlinear saturation. All nonlinear simulations discussed in this section use a collision frequency $\nu_{coll} = 0.00791\frac{C_s}{R_0}$, which is calculated with $Z_{eff} = 1$ and ion density n_{e0} and temperature T_{e0} described in section 3.1. This collision frequency is 10% of the linear growth rate in the absence of the equilibrium electric fields and causes a decrease of the ITG frequency by less than 2% and the linear growth rate by less than 7% for all cases.

We perform a series of nonlinear simulations of the $n = 20$ ITG using the same SOL geometry and constructed plasma profiles as linear simulations described in section 3.1. The zonal mode ($n = 0$) self-generated by the turbulence is artificially removed in these simulations to focus on the effects of equilibrium $E \times B$ shear flows. The time history of the volume-averaged ion heat conductivity is plotted in figure 8(a) for various shearing rates. The ITG modes first grow exponentially, then nonlinearly saturate due to the perturbed $E \times B$ drift. Similar to some studies in tokamaks, we simulate the nonlinear saturation and turbulent transport of a single toroidal mode, i.e. a 2D turbulence in the poloidal plane. The single-toroidal mode simulation provides a clear physics picture of effects of the equilibrium sheared flow, as we will see in our discussion that the mode structures are rather simple, and the mechanism of heat transport can be clearly addressed.

The simulations with different shearing rates ω_s have different growth rates and the instabilities saturate at different time steps in the simulations. For convenience of comparing their nonlinear saturations, we shift these cases horizontally so that they all saturate at the same time $t = 210R_0/C_s$. The heat conductivity is defined as $\chi = \frac{1}{n|\nabla T|}\int v_r \varepsilon \delta f d\boldsymbol{v}$, where v_r is the perturbed $E \times B$ drift across flux surface, ε is the particle kinetic energy. In this paper, χ is normalized by the Bohm unit $\rho_s^2\Omega_p = \frac{cT_{e0}}{eB_0}$, where $\rho_s = \frac{C_s}{\Omega_p}$. The heat transport leads to continuous increase in the amplitude of the perturbed distribution function $|\delta f/f|$, which could introduce a large particle noise. To make sure that the simulation results are not contaminated by particle noise, the noise-driven heat conductivity [44] is also plotted as the black dotted-dashed line in figure 8(a) for the case of $\omega_s = 0$, which shows that ITG transport (black solid line) is more than a thousand times larger than the noise-driven transport even though volume averaged $|\delta f/f| > 0.5$ at $t = 240R_0/C_s$.

5.1. Effects of E ×B shear on single-toroidal-mode ITG turbulence and transport in SOL

Figure 8(a) shows that the ITG with a larger shearing rate ω_s has a smaller growth rate and saturates with a lower fluctuation

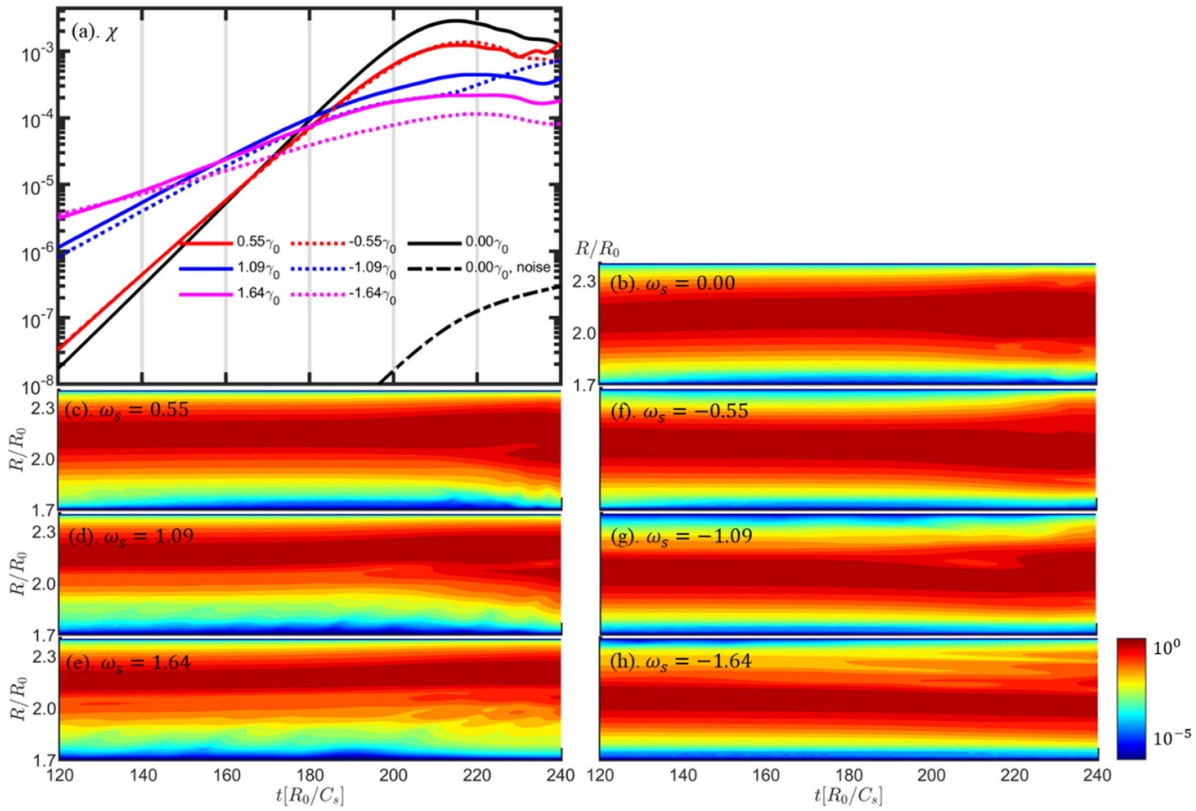

Figure 8. Panel (a): time evolution of ITG ion heat conductivity χ (volume-averaged) with various shearing rates ω_s. The noise-driven χ for the case of $\omega_s = 0.0$ is also plotted as the black dotted-dashed line. Panels (b)–(h): time evolution of radial profile of fluctuating potentials ($\delta\phi_{\rm rms}$) averaged over each flux surface and normalized by its maximal value at each time step.

amplitude and a smaller ion heat conductivity. For large shearing rates $\omega_s = 1.09$ and 1.64, the ITG saturates at slightly different levels between positive and negative ω_s. This breaking of symmetry with respect to the sign of ω_s arises from different nonlinear mode structures as shown in the panels (b)–(h) in figure 8. At each time step, the radial profile of the fluctuating potentials averaged over each flux surface ($\delta\phi_{\rm rms}$) is normalized by its maximal amplitude. The time-radial contour plots in figures 8(b)–(h) illustrate the evolution of the radial mode structure from linear to nonlinear phase. The radial mode structures are centrically peaked by the design of ion temperature gradients shown in figure 2. The reduction of the linear mode width due to the ω_s comes from the suppression of the mode at small R region for positive ω_s, but at large R region for negative ω_s. After nonlinear saturation, the ITG turbulence spreads radially [13, 42], primarily toward small R region for positive ω_s, but toward large R region for negative ω_s.

The nonlinear evolution of ITG mode structure in the SOL and turbulence spreading are illustrated in figures 9 and 10. The radial mode widths at the nonlinear saturation time $t = 210R_0/C_s$ are slightly larger than that of the linear eigenmodes in figure 4 The radial mode widths continue to increase at $t = 240R_0/C_s$ due to the turbulence spreading. In this single-toroidal-mode simulation, a single large eddy structure dominates in the simulation domain, which leads to highly fluctuating behaviors after the initial saturation of the ITG instability in figure 8(a). Instead of reaching a steady state, both the ion heat conductivity and mode structures continue to oscillate in the nonlinear phase. Other effects such as self-generated zonal flows, multiple toroidal modes, heat sources from FRC core region, and collisional effects may play a role in achieving a true steady state after the initial nonlinear saturation. We leave these interesting nonlinear physics to future studies, and in this work, we only focus on the effects of $E \times B$ sheared flows on the initial saturation point of the ITG modes.

The $E \times B$ sheared flows could suppress the ITG transport in the SOL by reducing both the turbulence intensity and eddy size. To estimate the radial eddy size, we calculate the two-point correlation function for the electrostatic potential at the nonlinear saturation $t = 210R_0/C_s$, $C_{R\zeta}(\Delta R, \Delta\zeta) = \frac{\langle\delta\phi(R,\zeta)\delta\phi(R+\Delta R,\zeta+\Delta\zeta)\rangle}{\sqrt{\langle\delta\phi(R,\zeta)^2\rangle\langle\delta\phi(R+\Delta R,\zeta+\Delta\zeta)^2\rangle}}$, where$\Delta R$ and $\Delta\zeta$ are spatial separation in the R and ζ direction, respectively, and $\langle\cdot\rangle$ represents averaging over the $Z = 0$ toroidal plane. Similar to Lin *et al* [27], we track the ridge of this 2D correlation function starting from $\Delta R = \Delta\zeta = 0$ to get a 1D radial correlation function $C_R(\Delta R)$. This is used to estimate the radial eddy size of Δr by noticing the fact that C_R decays like a Gaussian profile for small ΔR, i.e. $C_R(\Delta R) = C_{R0}\exp\left[-(\Delta R/\Delta r)^2\right]$. Figure 11(a) shows the dependency on the shearing rate for the radial eddy size Δr and the turbulence amplitude $\delta\phi_{\rm rms}$ averaged over the simulation volume at the time of the nonlinear saturation, i.e. before turbulence spreading. The reduction of the eddy size by the $E \times B$ shear is quite modest, up to 25%

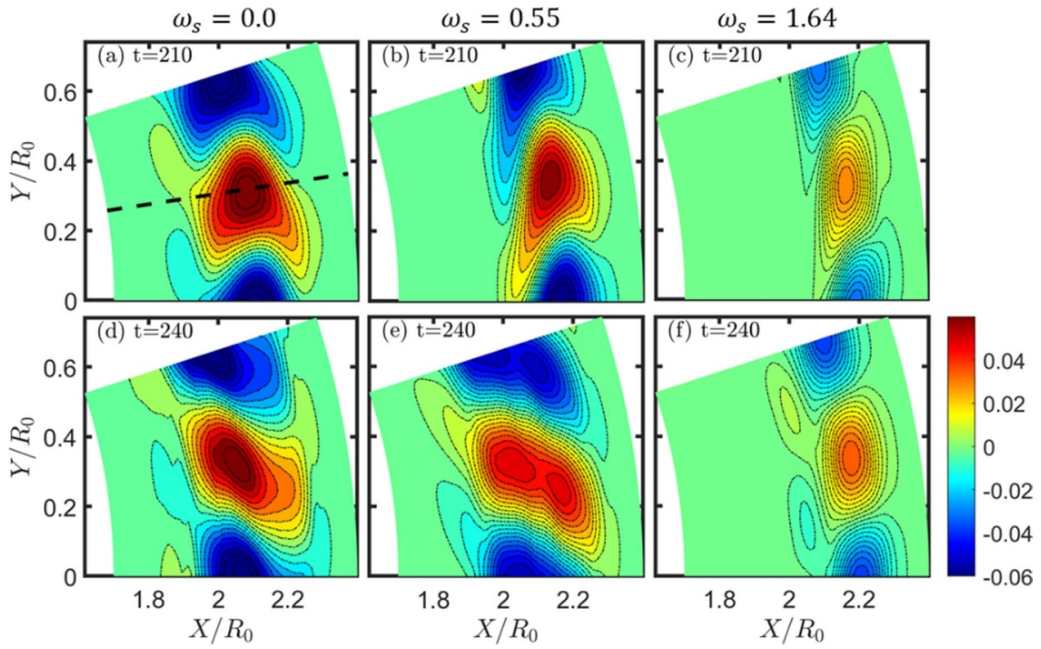

Figure 9. Contour plots of electrostatic potential $\delta\phi$ at the $Z = 0$ toroidal plane from GTC-X simulations in the SOL using various $E \times B$ shearing rates. Panels (a)–(c) are mode structures at saturation $t = 210R_0/C_s$. Panels (d)–(f) are mode structures at $t = 240R_0/C_s$ after nonlinear spreading. In panel (a), the dashed line is the middle plane that gives a cut for the poloidal plane appears in figure 10.

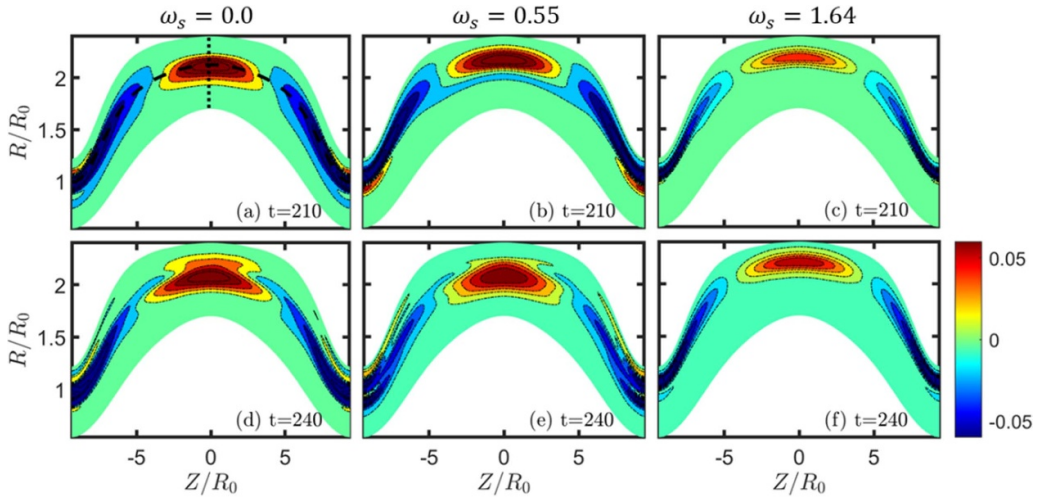

Figure 10. Contour plots of electrostatic potential $\delta\phi$ at the poloidal plane from GTC-X simulations in the SOL using various $E \times B$ shearing rates. Panels (a)–(c) are mode structures at saturation $t = 210R_0/C_s$. Panels (d)–(f) are mode structures at $t = 240R_0/C_s$ after nonlinear spreading. The dashed line in the panel (a) represents the flux surface of the maximum mode amplitude and the vertical dotted line gives the $Z = 0$ plane plotted in figure 9.

for the largest shearing rate. On the other hand, the reduction of the turbulence amplitude by the $E \times B$ shear is much more significant, up to 75% for the largest shearing rate. Both eddy size and turbulence amplitude exhibit a small asymmetry with respect to the sign of the shearing rate.

5.2. ITG saturation mechanism in SOL

Knowing the eddy size Δr and turbulence amplitude $\delta\phi_{\rm rms}$, we can estimate the eddy turnover time $\tau_{\rm eddy} = \frac{\Delta r}{\delta v_r}$, where the radial $E \times B$ drift is $\delta v_r = \frac{\delta E_\zeta}{B} = \frac{n\delta\phi_{\rm rms}}{\rm RB}$. Here we use the radial eddy size and radial drift to estimate the eddy turnover time since the eddy is nearly isotropic in the radial and toroidal directions. The dependence of the inverse of the eddy turnover time on the shearing rate is plotted in figure 11(b) together with the linear growth rate. The scaling of the growth rate is very similar to the inverse of the eddy turnover time. Indeed, table 1 shows that the eddy turnover time is only slightly larger than the inverse of the growth rate, except for the largest shearing rate. Furthermore, we observe that the eddy persists throughout the whole simulation time, so the eddy autocorrelation time $\tau_{\rm auto}$ is much longer than the eddy turnover time, i.e. large

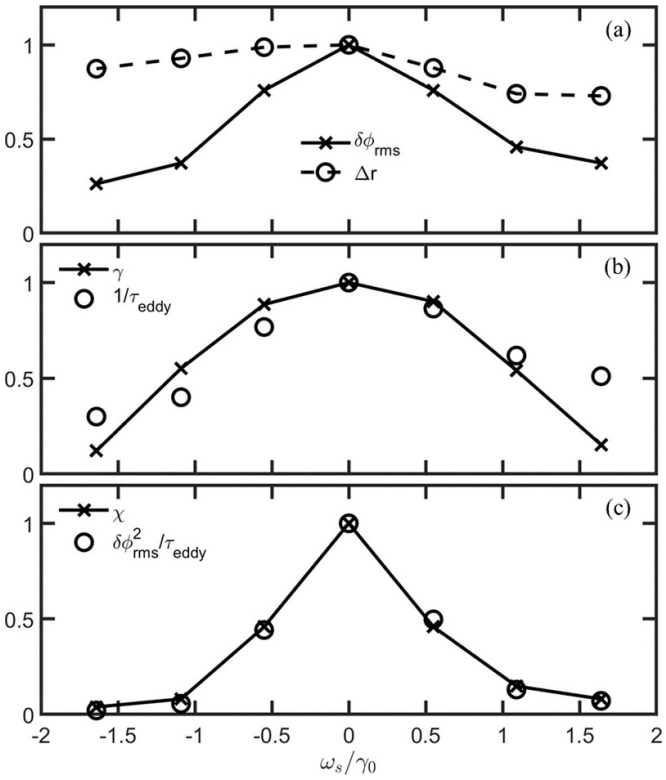

Figure 11. Dependence on the shearing rate for (panel (a)) ITG radial eddy size Δr and turbulence amplitude $\delta\phi_{\rm rms}$, (panel (b)) linear growth rate γ and inverse of eddy turnover time $\tau_{\rm eddy}$, and (panel c) the measured heat conductivity χ, and $\delta\phi^2_{\rm rms}/\tau_{\rm eddy}$ at the nonlinear saturation $t = 210R_0/C_{\rm s}$ from GTC-X simulations in the SOL. All quantities are normalized by their values for the case of $\omega_{\rm s} = 0$. Solid and dashed lines connect measured data points and indicate the scaling trend.

Table 1. Characteristic time scales for ITG turbulence with different shearing rate $\omega_{\rm s}$, the base case without shearing is highlighted with a grey background. All the quantities are in units $R_0/C_{\rm s}$.

$1/\omega_{\rm s}$	$\tau_{\rm decor}$	$\tau_{\|\|}$	τ_{rb}	$\tau_{\rm eddy}$	$1/\gamma$
8.6	3.0	3.6	464.6	37.3	92.4
12.9	3.6	3.6	261.5	30.8	26.1
25.7	4.1	3.6	118.4	22.1	15.7
∞	5.2	3.6	70.5	19.1	14.1
−25.7	4.1	3.6	149.9	24.8	15.9
−12.9	3.0	3.6	753.9	47.5	25.6
−8.6	2.9	3.6	1381.6	63.6	116.6

Kubo number regime. This is expected since the simulations treat only a single toroidal mode number $n = 20$. We conclude that the single-n ITG instability saturates when the inverse of the eddy turnover time is roughly equal to the linear growth rate, i.e. the saturation mechanism is the eddy rotation.

5.3. ITG transport mechanism in SOL

After establishing the eddy rotation as the ITG saturation mechanism, one would expect that the eddy rotation is also responsible for the turbulent transport. However, we find that a fluid calculation of ion heat conductivity χ based on a simple random walk model $\chi = \frac{\Delta r^2}{\tau_{\rm eddy}}$ predicts an ion heat conductivity much larger than that measured in the simulations, and even worse, the dependence of χ on the shearing rate does not match between the model and simulation results. In this random walk model, the eddy size is used as the spatial step size and the eddy turnover time is used as the time step size. Therefore, even though the fluid concept of eddy rotation is valid for the ITG saturation, it is not sufficient for the ITG transport.

To elucidate the kinetic origin for the transport mechanism, we define an effective decorrelation time $\tau_{\rm decor} = \frac{4\chi}{3\delta v_r^2}$ [27, 45]. We now search for a wave-particle decorrelation process that has a characteristic time scale comparable to this effective decorrelation time.

The guiding center parallel motion in SOL leads to a parallel wave-particle decorrelation time $\tau_{\|} = \frac{1}{k_{\|} v_{\rm th}}$, where $k_{\|}$ is approximated by the dominated $m = 1$ harmonics. The $\tau_{\|}$ characterizes the time scale for a particle to move across the eddy structure due to the parallel streaming, which is already found to be important in defining the mode frequency as discussed in section 3.1. Meanwhile, the guiding center radial diffusion responsible for the measured heat conductivity leads to a resonance broadening width of $1/\tau_{\rm rb}$, where $\tau_{\rm rb} = \frac{3\Delta r^2}{4\chi}$. We list these time scales in table 1 for various shearing rates. It is clear that the parallel wave-particle decorrelation time is very close to the effective wave-particle decorrelation, which is much shorter than the resonance broadening time and eddy turnover time. Therefore, the parallel wave-particle decorrelation should be the dominant transport mechanism.

Based on this transport mechanism, we can explain the dependence of the ion heat conductivity on the shearing rate using the random walk model. Since $\tau_{\|}$ is much smaller than the eddy turnover time $\tau_{\rm eddy}$, the guiding centers decorrelate from the eddy long before a full eddy rotation. Therefore, the guiding center radial excursion δr is due to the $E \times B$ drift in one parallel transit time, $\delta r = \delta v_r \tau_{||} = \frac{n\delta\phi_{\rm rms}}{k_{\|} v_{\rm th} {\rm RB}}$, which is much smaller than the eddy size Δr, i.e. $\delta r \ll \Delta r$. That is, the particle experiences a radial kick of δr distance whenever it travels across the mode in parallel direction. If the eddy is static, i.e. $\tau_{\rm eddy}$, $\tau_{\rm auto} \to \infty$, the guiding centers execute a periodic motion with a radial excursion length of δr, which does not lead to a radial diffusion. Therefore, the radial diffusion only arises due to the eddy rotation or decorrelation. Since $\tau_{\rm eddy} \ll \tau_{\rm auto}$, the $\tau_{\rm eddy}$ is the characteristic time scale for the radial diffusion and the δr is the characteristic length scale in a random walk process. This random walk model then gives rise to a scaling of the ion heat conductivity, $\chi = C\frac{\delta r^2}{\tau_{\rm eddy}} \propto \frac{\delta\phi^2_{\rm rms}}{\tau_{\rm eddy}}$. This scaling agrees very well with the measured ion heat conductivity as shown in figure 11(c) with $C = 5.5$.

Since the electron response is assumed to be adiabatic in these simulations, the ion particle flux is zero due to quasi-neutrality condition. The finite ion heat flux is induced by a process where ions with higher energy mostly diffuse outward but ions with lower energy mostly diffuse inward. The fact that the ion heat conductivity can be reasonably described by the

random walk model suggests that the ion transport induced by equilibrium shear flow can be a diffusive process.

6. Conclusion

In this paper, linear and nonlinear effects of an equilibrium radial electric field have been studied for the single-toroidal-mode ITG instability in the SOL region of an FRC geometry. New capabilities have been developed for the gyrokinetic particle code GTC-X to study the $E \times B$ sheared flow effects and an improved gyro-averaging scheme has implemented to capture the FLR effect for a single toroidal mode simulation for FRC.

After verifying the simulation results with a rigid $E \times B$ rotation, we first examined the linear effects of a constant radial $E \times B$ flow shear on ITG with $n = 20$ in the SOL while the Doppler shift of the mode frequency is minimized. We found that the ITG linear growth rate is strongly reduced, and the toroidal eddy shape is radially tilted by the $E \times B$ shear. Based on a slab model dispersion relation, the radial shear of the total local mode frequency is found to be important for the growth rate suppression. The maximal growth rate occurs when the radial shear of the Doppler shifted local mode frequency is zero.

In the nonlinear simulations, the $n = 20$ ITG saturation amplitude and heat transport level are greatly reduced by the $E \times B$ flow shear due to reduction of both turbulence intensity and eddy size. The turbulence intensity in the SOL is determined by the fluid eddy rotation, which is the dominant saturation mechanism since the growth rate is very similar to the inverse of the eddy turnover time. On the other hand, the effective decorrelation time responsible for the ion heat transport is closer to the parallel wave-particle decorrelation time. Before completing the whole circulation around the eddy, the particles already decorrelate from the wave due to parallel streaming in the SOL. A nicely fitted random walk model of ion heat conductivity with the particle radial excursion and the eddy turnover time further support these conclusions.

In the future work, we will extend our current study towards a more realistic FRC profile and investigate the heat load problem in FRC SOL. For example, we need to incorporate the self-generated zonal flows [8], which could have similar suppression effects as equilibrium $E \times B$ sheared flows on the ITG instability in the FRC SOL [46]. We also need to include multiple toroidal modes, which could induce nonlinear mode coupling leading to inverse spectral cascade [13]. Finally, we will carry out simulations with kinetic electrons and coupling the SOL with the core region, which provides a heat source for the SOL transport. We may need fully kinetic ions to incorporate the weak magnetic field regions such as magnetic separatrix and magnetic null in the FRC.

Data availability statement

The data that support the findings of this study are available upon reasonable request from the authors.

Acknowledgments

The authors would like to thank Dr Laura Galeotti for providing the FRC equilibrium data. This work was supported by TAE Grant No. TAE-200441, DOE SciDAC ISEP center, (T T) US DoE ECP (Exascale Computing Project), and (A K) BRNS Sanctioned No. 39/14/05/2018-BRNS and SERB Sanctioned No. EEQ/2017/000164. Simulations used resources on the Oak Ridge Leadership Computing Facility at Oak Ridge National Laboratory (DOE Contract No. DEAC05-00OR22725) and the National Energy Research Scientific Computing Center (DOE Contract No. DE-AC02-05CH11231).

ORCID iDs

W H Wang https://orcid.org/0000-0001-8743-0430
X S Wei https://orcid.org/0000-0001-7486-0407
G J Choi https://orcid.org/0000-0003-0044-1650
A Kuley https://orcid.org/0000-0003-2325-6597
C Lau https://orcid.org/0000-0001-6702-1461

References

[1] Tuszewski M 1988 Field reversed configurations *Nucl. Fusion* **28** 2033
[2] Binderbauer M W *et al* 2015 A high performance field-reversed configuration *Phys. Plasmas* **22** 056110
[3] Guo H Y *et al* 2015 Achieving a long-lived high-beta plasma state by energetic beam injection *Nat. Commun.* **6** 1–6
[4] Gota H *et al* 2019 Formation of hot, stable, long-lived field-reversed configuration plasmas on the C-2W device *Nucl. Fusion* **59** 112009
[5] Tuszewski M *et al* 2012 Field reversed configuration confinement enhancement through edge biasing and neutral beam injection *Phys. Rev. Lett.* **108** 255008
[6] Rosenbluth M N, Krall N A and Rostoker N 1962 Finite Larmor radius stabilization of 'weakly' unstable confined plasmas (No. GA-2371) General Dynamics Corp., San Diego, CA (available at: www.osti.gov/biblio/4808729)
[7] Schmitz L *et al* 2016 Suppressed ion-scale turbulence in a hot high-β plasma *Nat. Commun.* **7** 1–11
[8] Lin Z, Hahm T S, Lee W W, Tang W M and White R B 1998 Turbulent transport reduction by zonal flows: massively parallel simulations *Science* **281** 1835–7
[9] Fulton D P, Lau C K, Holod I, Lin Z and Dettrick S 2016 Gyrokinetic particle simulation of a field reversed configuration *Phys. Plasmas* **23** 012509
[10] Fulton D P, Lau C K, Schmitz L, Holod I, Lin Z, Tajima T, Binderbauer M W and Team T A E 2016 Gyrokinetic simulation of driftwave instability in field-reversed configuration *Phys. Plasmas* **23** 056111
[11] Lau C K, Fulton D P, Holod I, Lin Z, Binderbauer M, Tajima T and Schmitz L 2017 Drift-wave stability in the field-reversed configuration *Phys. Plasmas* **24** 082512
[12] Lau C 2017 Electrostatic turbulence and transport in the field-reversed configuration Doctoral Dissertation UC Irvine
[13] Lau C K, Fulton D P, Bao J, Lin Z, Tajima T, Schmitz L, Dettrick S and (TAE Team) 2019 Cross-separatrix simulations of turbulent transport in the field-reversed configuration *Nucl. Fusion* **59** 066018
[14] Lau C K, Fulton D P, Bao J, Lin Z, Dettrick S, Binderbauer M, Tajima T and Schmitz L 2020 Electrostatic quasi-neutral formulation of global cross-separatrix particle simulation in

field-reversed configuration geometry *Phys. Plasmas* **27** 082504
[15] Bao J, Lau C K, Lin Z, Wang H Y, Fulton D P, Dettrick S and Tajima T 2019 Global simulation of ion temperature gradient instabilities in a field-reversed configuration *Phys. Plasmas* **26** 042506
[16] Biglari H, Diamond P H and Terry P W 1990 Influence of sheared poloidal rotation on edge turbulence *Phys. Fluids* B **2** 1–4
[17] Hahm T S and Burrell K H 1995 Flow shear induced fluctuation suppression in finite aspect ratio shaped tokamak plasma *Phys. Plasmas* **2** 1648–51
[18] Kishimoto Y, Tajima T, Horton W, LeBrun M J and Kim J Y 1996 Theory of self-organized critical transport in tokamak plasmas *Phys. Plasmas* **3** 1289–307
[19] Burrell K H 1997 Effects of $E\times B$ velocity shear and magnetic shear on turbulence and transport in magnetic confinement devices *Phys. Plasmas* **4** 1499–518
[20] Connor J W, Taylor J B and Wilson H R 1993 Shear damping of drift waves in toroidal plasmas *Phys. Rev. Lett.* **70** 1803
[21] Taylor J B and Wilson H R 1996 Plasma rotation and toroidal drift modes *Plasma Phys. Control. Fusion* **38** 1999
[22] Waltz R E, Dewar R L and Garbet X 1998 Theory and simulation of rotational shear stabilization of turbulence *Phys. Plasmas* **5** 1784–92
[23] Hill P, Saarelma S, McMillan B, Peeters A and Verwichte E 2012 Perpendicular wavenumber dependence of the linear stability of global ion temperature gradient modes on $E \times B$ flows *Plasma Phys. Control. Fusion* **54** 065011
[24] Abdoul P A, Dickinson D, Roach C M and Wilson H R 2015 Using a local gyrokinetic code to study global ion temperature gradient modes in tokamaks *Plasma Phys. Control. Fusion* **57** 065004
[25] Chen L, Lin Z and White R 2000 Excitation of zonal flow by drift waves in toroidal plasmas *Phys. Plasmas* **7** 3129–32
[26] Diamond P H, Itoh S I, Itoh K and Hahm T S 2005 Zonal flows in plasma—a review *Plasma Phys. Control. Fusion* **47** R35
[27] Lin Z, Holod I, Chen L, Diamond P H, Hahm T S and Ethier S 2007 Wave-particle decorrelation and transport of anisotropic turbulence in collisionless plasmas *Phys. Rev. Lett.* **99** 265003
[28] Lee W W 1983 Gyrokinetic approach in particle simulation *Phys. Fluids* **26** 556–62
[29] Tajima T 1989 *Computational Plasma Physics: With Applications to Fusion and Astrophysics* (*Benjamin Frontier Series*) (Reading, MA: Addison-Wesley) p 254–66
[30] Parker S E and Lee W W 1993 A fully nonlinear characteristic method for gyrokinetic simulation *Phys. Fluids* B **5** 77–86
[31] Dimits A M and Lee W W 1993 Partially linearized algorithms in gyrokinetic particle simulation *J. Comput. Phys.* **107** 309–23
[32] Hu G and Krommes J A 1994 Generalized weighting scheme for δf particle-simulation method *Phys. Plasmas* **1** 863–74
[33] Lee W W 1987 Gyrokinetic particle simulation model *J. Comput. Phys.* **72** 243–69
[34] Lin Z and Lee W W 1995 Method for solving the gyrokinetic Poisson equation in general geometry *Phys. Rev.* E **52** 5646
[35] Brizard A J 1995 Nonlinear gyrokinetic Vlasov equation for toroidally rotating axisymmetric tokamaks *Phys. Plasmas* **2** 459–71
[36] Hahm T S 1996 Nonlinear gyrokinetic equations for turbulence in core transport barriers *Phys. Plasmas* **3** 4658–64
[37] Brizard A and Hahm T 2007 Foundations of nonlinear gyrokinetic theory *Rev. Mod. Phys.* **79** 421
[38] Galeotti L, Barnes D C Ceccherini F and Pegoraro F 2011 Plasma equilibria with multiple ion species: equations and algorithm *Phys. Plasmas* **18** 082509
[39] Sun S, Wei X, Lin Z, Liu P, Wang W and Xie H 2020 Verification of local electrostatic gyrokinetic simulation of drift-wave instability in field-reversed configuration *Phys. Plasmas* **27** 112504
[40] Taimourzadeh S, Shi L, Lin Z, Nazikian R, Holod I and Spong D A 2019 Effects of RMP-induced changes of radial electric fields on microturbulence in DIII-D tokamak pedestal top *Nucl. Fusion* **59** 046005
[41] Carlstrom T N, Groebner R J, Fenzi C, McKee G R, Moyer R A and Rhodes T L 2002 Evidence for the role of velocity shear on the LH transition in DIII-D *Plasma Phys. Control. Fusion* **44** A333
[42] Lin Z and Hahm T S 2004 Turbulence spreading and transport scaling in global gyrokinetic particle simulations *Phys. Plasmas* **11** 1099–108
[43] Lin Z, Tang W M and Lee W W 1995 Gyrokinetic particle simulation of neoclassical transport *Phys. Plasmas* **2** 2975–88
[44] Holod I and Lin Z 2007 Statistical analysis of fluctuations and noise-driven transport in particle-in-cell simulations of plasma turbulence *Phys. Plasmas* **14** 032306
[45] Xiao Y and Lin Z 2009 Turbulent transport of trapped-electron modes in collisionless plasmas *Phys. Rev. Lett.* **103** 085004
[46] Wei X S *et al* 2021 Effects of zonal flows on ion temperature gradient instability in the scrape-off layer of a field-reversed configuration (in preparation)